# Theory of ionization in a crystal with a linear and a circular laser polarization: Influence of the laser wavelength

Rachel Nuter
*CEA-CESTA, F-33116 Le Barp Cedex, France*

(Received 9 June 2023; revised 31 July 2023; accepted 10 August 2023; published 1 September 2023; corrected 4 October 2023)

We consider the theoretical formalism presented by Otobe *et al.* [J. Phys. Soc. Jpn, **88**, 024706 (2019)] to write the photoionization rate of a crystal irradiated by a linearly and a circularly polarized laser beam valid in low- and high-intensity regimes. We expand these analytical expressions in the multiphoton regime corresponding to the low laser intensity domain. This provides a theoretical formulation for the photoionization cross section valid for a linear and a circular laser polarization. Whereas the quartz crystal produces a larger charge density when it is irradiated with an 800-nm linearly polarized laser beam than a circularly polarized one, no difference in ionization rate is noticeable when the laser wavelength is equal to 351 nm.

DOI: 10.1103/PhysRevA.108.033101

## I. INTRODUCTION

The ionization of solids by a laser field is a fundamental process occurring in the laser-matter interaction topic [1,2]. It is involved in a large domain of applications ranging from femtosecond laser ablation [3] to laser damage [4,5] and glass laser cutting [6]. The photoionization is a key process in the laser damage as it occurs over the first interaction instants, when the laser intensity is sufficiently high to generate a microplasma. Ionization processes of optical components are mostly studied by considering a linearly polarized laser beam. Very little research exists on the use of a circularly polarized laser beam in the ionization of dielectric bulks.

From a theoretical point of view, the photoionization of solids used to be modeled with the well-known Keldysh theory for crystal [7,8]. This theory computes the probability to promote an electron from the valence to the conduction band in a two-band system by neglecting the intraband coupling terms. It presents the advantage to provide an analytical expression for the ionization rate valid in both multiphoton (low-intensity domain) and tunnel (high-intensity domain) regimes. However, this theory is only valid for a linearly polarized laser beam, and should not be applied to different laser polarizations, such as, for example, circular polarization. Indeed, by irradiating sapphire and fused silica crystals with an 800-nm laser field, Temnov *et al.* [9] have experimentally measured that the produced charge density is higher for a linear polarization than for a circular polarization.

Few theories have been developed for the ionization of a crystal with a circularly polarized laser beam [10–12]. Jones and Reiss [11] have considered Volkov-type functions to model the electronic wave function in the valence and the conduction bands. They provide a theoretical expression for the ionization rate depending on the dipole matrix element such that no analytical formula is available. The most advanced photoionization theory of a crystal irradiated by a circularly polarized laser beam has been developed by Otobe *et al.* in [12]. Their formalism is similar to the one used by Keldysh [7], which means they consider Houston functions [13] to model the electronic wave functions. In contrast to the Keldysh work, they use a parabolic two-band system to model the solid band structure. The Otobe's theory confirms the experimental measurements made by Temnov *et al.* [9], which is a higher ionization rate for linear polarization than for circular polarization for a quartz crystal irradiated by an 800-nm laser field. However, they do not provide a theoretical formula for the photo-ionization cross section, a simplified expression of the photoionization rate usually considered in the low-intensity regime.

In this work, we consider the Otobe's formalism [12] to compute the ionization rate of a crystal irradiated by a linearly or a circularly polarized laser beam. Our analytical expressions for the ionization probabilities slightly differ from the Otobe's formula [12]. We are interested in the crystal ionization in the multiphoton regime (MPI regime), where the ionization rate is proportional to a power of the laser intensity, $I^n$, where $n$ is the number of photons needed to make electron transit from the valence to the conduction band and $I$ is the laser beam intensity. This regime is reached for a Keldysh parameter [7] much larger than 1. By performing a development of the ionization rate formula in the multiphoton regime, we provide an analytical expression for the photoionization cross section valid for linear or circular polarization. This formula is a useful simplified expression of the photoionization rate for the solid ionization studies. By computing the ionization rate of a quartz crystal irradiated by an 800-nm laser field, we note that circular polarization shows a different behavior in the multiphoton regime than the linear polarization. Nonetheless, we retrieve for this laser wavelength, a higher ionization probability for the linearly polarized laser beam, as was presented in [9,12]. We also evaluate the photoionization probability of a quartz irradiated by an ultraviolet (UV) laser beam ($\lambda = 351$ nm), where this wavelength corresponds to the third harmonic of the Laser MegaJoule (LMJ) facility [14]. For this case, where only three photons are needed to ionize the crystal, no difference is noticeable in the ionization rate between the two laser polarizations. Finally, we apply our theoretical development to the experimental measurements

 

of free-carrier density reported by Temnov *et al.* in [9]. The theory reproduces the experimental observation, which is a higher free-carrier density for a bulk irradiated by a linearly polarized laser beam than by a circularly polarized one.

## II. THEORETICAL EXPRESSION FOR THE CRYSTAL IONIZATION RATE

Otobe *et al.* [12] have detailed the theoretical development of the ionization rates for a crystal irradiated by a linearly or a circularly polarized laser beam. Their formalism lies on the following hypothesis:

(1) The Houston functions [13] model the electronic wave functions in the valence and conduction bands. Note that these functions were also considered by Keldysh in [7].

(2) The band structure of the crystal is modeled with a parabolic two-band system widely used for description of the central part of the Brillouin zone and considered as a standard approximation in many problems of solid-state physics [15].

(3) The laser beam is modeled with a plane wave.

This theoretical development is detailed in Appendix A where our formula slightly differs from the Otobe's formula.

We express the photoionization rates as a function of the Keldysh parameter [7], $\gamma = \frac{\omega\sqrt{\mu_r B_g}}{eE_0}$, with $\mu_r$ the reduced electron-hole mass, $B_g$ the band gap of the crystal, $e$ the electron charge, $\omega$ the photon angular frequency, and $E_0$ the laser electric field amplitude. Thus, the photoionization rate for linear polarization expressed per time and volume units writes as

$$
\begin{aligned}
W_{\text{lin}} &= \frac{1}{16\sqrt{2}\pi}\frac{1}{\gamma^2}\frac{\mu_r^{3/2}\omega^4\sqrt{B_g}}{(\hbar\omega)^2}\int_0^\pi \sin\theta\, d\theta \\
&\quad\times\sum_{l\geqslant l_0}\sqrt{\frac{l\hbar\omega}{B_g}-1-\frac{1}{4\gamma^2}}\left[\overline{J_{l-1}}(\alpha,\beta)-\overline{J_{l+1}}(\alpha,\beta)\right]^2, \\
\alpha &= -\frac{\sqrt{2}}{\gamma}\frac{B_g}{\hbar\omega}\sqrt{\frac{l\hbar\omega}{B_g}-1-\frac{1}{4\gamma^2}}\cos\theta, \\
\beta &= -\frac{1}{8\gamma^2}\frac{B_g}{\hbar\omega}, \\
l_0 &= \min_l\left(\frac{l\hbar\omega}{B_g}-1-\frac{1}{4\gamma^2}>0\right),
\end{aligned}
\tag{1}
$$

where $\overline{J_n}(u,v)$ are the generalized Bessel functions [16]. The photoionization rate formula sums the $l$-photon processes allowing electrons to transit from the valence to the conduction band. The $l$ sum starts from $l_0$ corresponding to the minimum number of photons needed to make electrons transit to the conduction band. Under the influence of a linearly polarized laser beam, the band gap is broadened by the ponderomotive energy equal to $\frac{B_g}{4\gamma^2}$.

For a circular laser polarization, the photoionization rate writes as

$$
\begin{aligned}
W_{\text{cir}} &= \frac{1}{8\sqrt{2}\pi}\frac{1}{\gamma^2}\frac{\mu_r^{3/2}\omega^4\sqrt{B_g}}{(\hbar\omega)^2}\int_0^\pi \sin\theta\, d\theta \\
&\quad\times\sum_{l\geqslant l_0}\sqrt{\frac{l\hbar\omega}{B_g}-1-\frac{1}{2\gamma^2}}\left[J_{l-1}^2(\eta)+J_{l+1}^2(\eta)\right],
\end{aligned}
$$

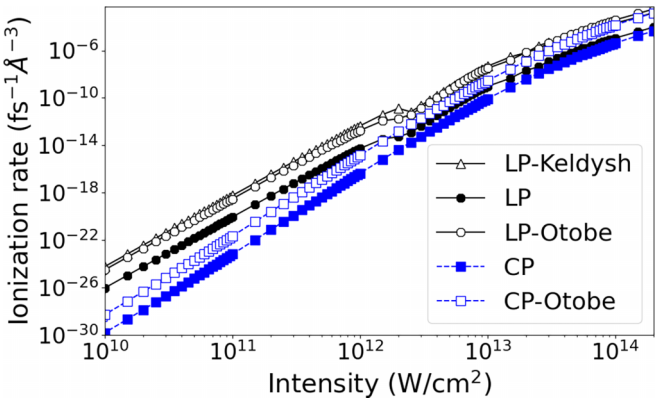


FIG. 1. Ionization rate versus the laser intensity for linear polarization (LP) computed from the Keldysh theory (triangles), the Otobe's theory (empty circles), and Eq. (1) (filled circles), and for circular polarization (CP) computed from the Otobe's theory (empty squares) and Eq. (2) (filled squares).

$$
\begin{aligned}
\eta &= -\frac{\sqrt{2}}{\gamma}\frac{B_g}{\hbar\omega}\sqrt{\frac{l\hbar\omega}{B_g}-1-\frac{1}{2\gamma^2}}\sin\theta, \\
l_0 &= \min_l\left(\frac{l\hbar\omega}{B_g}-1-\frac{1}{2\gamma^2}>0\right),
\end{aligned}
\tag{2}
$$

where $J_l(x)$ denotes the Bessel functions of the first kind [17]. In this case, the ponderomotive energy is larger than in the linear case; it is equal to $\frac{B_g}{2\gamma^2}$. To illustrate our theoretical formalism, we apply it to a quartz crystal characterized by a band gap $B_g = 9$ eV and a reduced hole-electron mass $\mu_r = 0.3m_e$, with $m_e$ the electron mass. We set the laser wavelength equal to 800 nm resulting in a linear refractive index equal to $n_0 = 1.4533$ [18]. Figure 1 illustrates the quartz photoionization rate for a linear (triangles and circles) and a circular (squares) laser beam polarization as a function of the laser intensity. Our formalism (filled circles and squares) is compared to the Otobe's formalism [12] (empty circles and squares) and the Keldsyh's formalism [7] (triangles). As explained in Appendix A, our results are lower than Otobe's results by a factor equal to 34, originating from the $(\frac{\hbar\omega}{B_g})^2$ factor. Nonetheless, we observe for this laser wavelength, a higher ionization probability for the linear polarization than for the circular polarization; four orders of magnitude separate the two ionization rates in the low laser intensity regime. We retrieve the well-known behavior of the ionization probability in this regime, which is $W = \sigma^{(n)}I^n$, where $\sigma^{(n)}$ is the photoionization cross section, and $n$ is the number of photons needed to ionize the quartz crystal.

For a linear polarization, we retrieve the well-known behavior of the intensity-dependent ionization rate: a slope break near $I \sim 10^{12}$ W/cm$^2$, originating from a transition between the six-photon regime to the seven-photon regime resulting from the band gap broadened by the ponderomotive energy ($\sim\frac{B_g}{4\gamma^2}$). This slope break is not present for a circular polarization displaying a homogeneous curve. This feature is detailed in the next section.

The analytical development presented in Appendix A shows that the ionization rate for a crystal depends on the

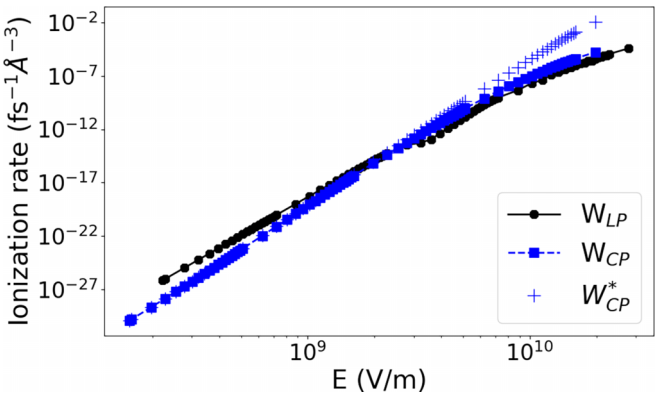


FIG. 2. Ionization rate versus the electric field for linear polarization ($W_{LP}$) computed from Eq. (1) (filled circles), and for circular polarization ($W_{CP}$) computed from Eq. (2) (filled squares). $W^{*}_{CP}$ (crosses) is obtained from Eq. (2) by considering $U_P = \frac{B_g}{4\gamma^2}$. $\lambda = 800$ nm.

electric field amplitude of the laser beam. Because the relation between the laser intensity and the electric field changes with the laser polarization (see Appendix B), it is meaningful to draw in Fig. 2 the ionization rate versus the electric field for linear (black circle) and circular (blue square) polarization. Blue crosses display the ionization rate for circular polarization computed by considering that the ponderomotive energy experienced by the electron is equal to that evaluated for linear polarization, which is $U_P = \frac{B_g}{4\gamma^2}$. This substitution in Eq. (2) ensures a similar broadened band gap for both laser polarizations. The electric field values presented in this figure correspond to laser intensity values ranging from $10^{10}$ to $10^{14}$ W/cm$^2$.

In the low laser intensity regime, we still observe an ionization rate for linear polarization higher than for the circular polarization. We could think that the polarization-dependent ponderomotive energy experienced by the electron has an impact on this difference. However, no difference exists between the crosses ($U_P = \frac{B_g}{4\gamma^2}$) and the squares ($U_P = \frac{B_g}{2\gamma^2}$), meaning that the dominance of LP on the ionization rate does not result for the lower value of its associated ponderomotive energy. This polarization-dependent ionization rate dynamics is similar to the theoretical results presented for atom ionization in the multiphoton regime [19]. In this case, the higher ionization rate for linear polarization originates from the difference in the selection rule for the quantum magnetic number $\Delta m$, that is, $\Delta m = 0$ for the linear polarization and $\Delta m = +1(\Delta m = -1)$ for the left (right) circular polarization. This last selection rule reduces the number of allowed electronic transition channels for circular polarization resulting in a lower ionization rate. Similar dynamics may be applied for solids ionization in the low intensity regime; this requires additional theoretical developments. When the ionization rate slope breaks for linear polarization, we observe in Fig. 2 a higher ionization rate for circular polarization, in a similar fashion as for the ionization rate for atomic systems in the tunnel regime [20,21]. Once again, this difference does not originate from the polarization-dependent ponderomotive energy.

These results show that the domination of the linear polarization over the circular polarization in the photoionization process mainly originates from the difference in the laser intensity computation (see Appendix B).

## III. MULTIPHOTON REGIME

Because we are interested by the low laser intensity regime, we theoretically compute the ionization cross section $\sigma^{(n)}$. This regime, usually called the multiphoton ionization regime (MPI), is reached when the Keldysh parameter is larger than 1 ($\gamma \gg 1$).

### A. Linear polarization

We compute the ionization rate in the $l_0$ regime:

$$W_{\text{lin}}^{\text{MPI}} = \frac{1}{16\sqrt{2}\pi}\frac{\mu_r^{3/2}\omega^2}{\hbar^2\gamma^2}\sqrt{B_g}\sqrt{\frac{l_0\hbar\omega}{B_g}-1} \times \int_0^{\pi}\sin\theta\, d\theta[\overline{J}_{l_0-1}(\tilde{\alpha},\beta)-\overline{J}_{l_0+1}(\tilde{\alpha},\beta)]^2,$$
$$\tilde{\alpha} = -\frac{\sqrt{2}}{\gamma}\frac{B_g}{\hbar\omega}\sqrt{\frac{l_0\hbar\omega}{B_g}-1}\cos\theta. \tag{3}$$

For $|x| \ll 1$, the Bessel function is approximated by $J_n(x) = \frac{1}{\Gamma(n+1)}(\frac{x}{2})^n$ where $\Gamma(x)$ is the gamma function [17]. As $\gamma \gg 1$, we have $\tilde{\alpha} \ll 1$ and $\beta \ll 1$, such that the generalized Bessel function could be approximated by

$$J_n(\tilde{\alpha},\beta) = \frac{(\frac{\tilde{\alpha}}{2})^n}{\Gamma(n+1)} + \sum_{k=1}^{+\infty}\left[\frac{(\frac{\beta}{2})^k}{\Gamma(k+1)} \times \left(\frac{(\frac{\tilde{\alpha}}{2})^{n-2k}}{\Gamma(n-2k+1)} + (-1)^k\frac{(\frac{\tilde{\alpha}}{2})^{n+2k}}{\Gamma(n+2k+1)}\right)\right]. \tag{4}$$

By considering the intensity formula for the linearly polarized laser beam, $I_0 = \frac{1}{2}\epsilon_0 c n_0 |E_0|^2$ (see Appendix B), we obtain

$$W_{\text{lin}}^{\text{MPI}} = \sigma_{\text{lin}}^{(n)} I_0^n, \quad \sigma_{\text{lin}}^{(n)} = \frac{1}{2^{5/2}\pi}\frac{1}{[\Gamma(n)]^2}\frac{1}{2n-1}\left(\frac{B_g}{\mu_r}\right)^{n-(3/2)}\frac{(\hbar\omega)^{4-4n}}{\hbar^{4-2n}}\left[\frac{n\hbar\omega}{B_g}-1\right]^{n-(1/2)}\left(\frac{e^2}{\epsilon_0 c n_0}\right)^n\phi,$$
$$\phi = 1 + 2\sum_{k=1}^{+\infty}\frac{\Gamma(n)}{\Gamma(k+1)\Gamma(n-2k)}\frac{2n-1}{2n-1-2k}\left[\frac{-\frac{1}{8}}{\frac{B_g}{\hbar\omega}\left(\frac{n\hbar\omega}{B_g}-1\right)}\right]^k + \sum_{k,k'=1}^{+\infty}\frac{[\Gamma(n)]^2}{\Gamma(k+1)\Gamma(k'+1)\Gamma(n-2k)\Gamma(n-2k')} \times \frac{2n-1}{2n-1-2(k+k')}\left[\frac{-\frac{1}{8}}{\frac{B_g}{\hbar\omega}\left(\frac{n\hbar\omega}{B_g}-1\right)}\right]^{k+k'}. \tag{5}$$

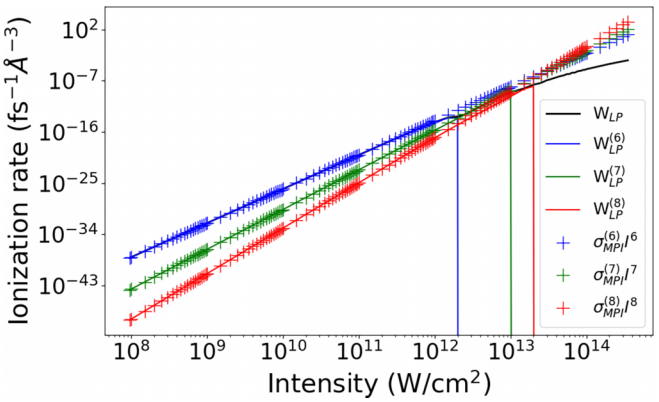


FIG. 3. Quartz ionization rate versus the laser intensity for an 800-nm linearly polarized (LP) laser beam: full formula (black solid curve), six-photon (blue solid curve), seven-photon (green solid curve), and eight-photon (red solid curve) regimes; MPI formula for six-photon (blue crosses), seven-photon (green crosses), and eight-photon (red crosses) regimes.

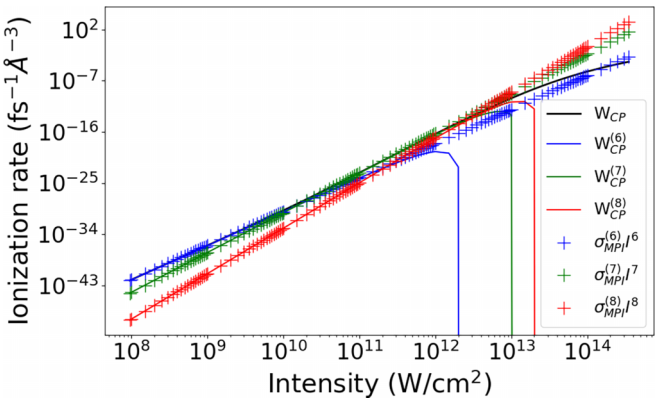


FIG. 4. Quartz ionization rate versus the laser intensity for an 800-nm circularly polarized laser beam (CP): full formula (black solid curve), six-photon (blue solid curve), seven-photon (green solid curve), and eight-photon (red solid curve) regimes; MPI formula for six-photon (blue crosses), seven-photon (green crosses), and eight-photon (red crosses) regimes.

These computations are illustrated in Fig. 3 drawing the ionization rate of a quartz crystal with an 800-nm linearly polarized laser beam. The full formula [Eq. (1), black solid curve] is compared with the six-photon ($W_{LP}^{(6)}$, blue solid curve), the seven-photon ($W_{LP}^{(7)}$, green solid curve), and the eight-photon ($W_{LP}^{(8)}$, red solid curve) regimes. Note that the $W_{LP}^{(n)}$ term, corresponding to the ionization probability of the $n$-photon transition, is extracted from Eq. (1).

For a laser intensity lower than $10^{12}$ W/cm$^2$, the ionization probability is dominated by the six-photon regime. At these intensity values, the seven-photon and eight-photon processes display a much weaker ionization probability; the $W_{LP}^{(6)}$ term is the dominant term in the ionization rate. As the laser intensity value increases, the ponderomotive energy broadens the crystal band gap resulting in a six-photon regime saturation near a laser intensity equal to $10^{12}$ W/cm$^2$. For an intensity equal to $2 \times 10^{12}$ W/cm$^2$, $W_{LP}^{(6)}$ is zero: the ponderomotive energy is so strong that the broadened band gap no longer allows a six-photon process to make the electron transit from the valence to the conduction bands. For a laser intensity higher than $2 \times 10^{12}$ W/cm$^2$, the seven-photon process becomes the dominant process in the quartz ionization. This regime transition leads to a slope break in the ionization rate curve. Similar behavior is observed with higher laser intensities for the seven- to eight-photon regime transition.

The blue, green, and red crosses draw the ionization rate computed from the MPI formula [Eq. (5)] for the six-, seven- and eight-photon processes, respectively. From a numerical point of view, the $k$ sum in the MPI formula converges for $k = 2$ for the six-photon regime and $k = 3$ for the seven- and eight-photon regimes. The MPI photoionization formula reproduces perfectly the $n$-photon processes up to its zero value. The MPI formula could then be used to model the quartz photoionization process in the low-intensity regime.

### B. Circular polarization

As previously, we assume that the multiphoton regime ($\gamma \gg 1$) is dominated by the $l_0$ regime:

$$W_{\text{cir}}^{\text{MPI}} = \frac{1}{8\sqrt{2}\pi} \frac{\mu_r^{3/2}\omega^4\sqrt{B_g}}{(\hbar\omega)^2\gamma^2} \int_0^\pi \sin\theta\, d\theta \times \sqrt{\frac{l_0\hbar\omega}{B_g} - 1} \left[J_{l_0-1}^2(\tilde{\eta}) + J_{l_0+1}^2(\tilde{\eta})\right],$$
$$\tilde{\eta} = -\frac{\sqrt{2}}{\gamma}\frac{B_g}{\hbar\omega}\sqrt{\frac{l_0\hbar\omega}{B_g} - 1}\,\sin\theta. \tag{6}$$

As $\gamma \gg 1$, $\tilde{\eta} \ll 1$ such that we consider the zero limit of the Bessel function: $J_n(x) = \frac{1}{\Gamma(n+1)}(\frac{x}{2})^n$. The MPI limit then reduces to

$$W_{\text{cir}}^{\text{MPI}} = \frac{1}{8\sqrt{2}\pi} \frac{\mu_r^{3/2}\omega^4\sqrt{B_g}}{(\hbar\omega)^2\gamma^2} \frac{\sqrt{\frac{l_0\hbar\omega}{B_g} - 1}}{[\Gamma(l_0)]^2} \int_0^\pi \sin\theta \left(\frac{\tilde{\eta}}{2}\right)^{2l_0-2} d\theta. \tag{7}$$

By considering the Wallis formula $\int_0^{\pi/2} \sin^{2n} x\, dx = \frac{\sqrt{\pi}}{2}\frac{\Gamma(n+\frac{1}{2})}{\Gamma(n+1)}$, and the laser intensity expression $I_0 = \epsilon_0 c n_0 |E_0|^2$ for a circularly polarized laser beam (see Appendix B), we obtain

$$W_{\text{cir}}^{\text{MPI}} = \sigma_{\text{cir}}^{(n)} I_0^n,$$
$$\sigma_{\text{cir}}^{(n)} = \frac{1}{\sqrt{\pi}}\frac{1}{2^{n+(5/2)}}\frac{1}{\Gamma(n)\Gamma\left(n+\frac{1}{2}\right)}\frac{(\hbar\omega)^{4-4n}}{\hbar^{4-2n}}\left(\frac{B_g}{\mu_r}\right)^{n-(3/2)} \times \left(\frac{n\hbar\omega}{B_g} - 1\right)^{n-(1/2)} \frac{e^{2n}}{(\epsilon_0 c n_0)^n}. \tag{8}$$

Figure 4 computes the photoionization rates of crystal with an 800-nm circularly polarized laser beam with different formula. As previously, we note that in the low-intensity regime, the ionization rate is dominated by the six-photon

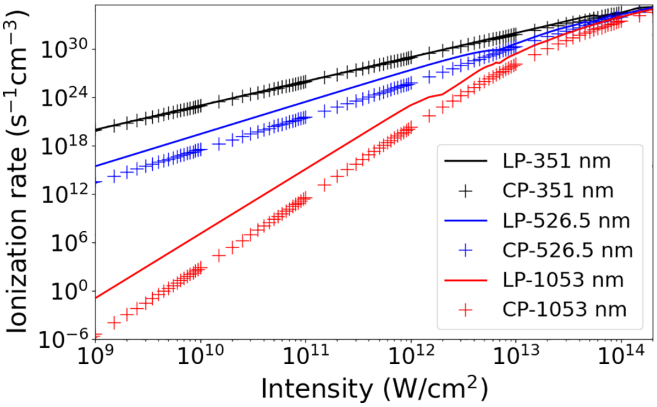


FIG. 5. Quartz ionization rate with a linear (solid curve) and circular (crosses) polarization for three values of laser wavelength: $\lambda = 351$ nm (black), $\lambda = 526.5$ nm (blue), and $\lambda = 1053$ nm (red).

process. Whereas the six-photon process domination occurs up to an intensity equal to $10^{12}$ W/cm$^2$ in the case of linear polarization, we observe that for circular polarization, it only dominates up to an intensity equal to $10^{10}$ W/cm$^2$. Moreover, in contrast to the linear case, we observe that the seven-photon process dominates the ionization rate whereas the six-photon process still enables an electron transition from the valence to the conduction bands. The photoionization dynamics with a circularly polarized laser beam differs from the linear one as it allows the coexistence of two $n$-photon processes in the low laser intensity regime. Thus, the MPI formula for the circular polarization should be carefully used: for some laser intensity values, the MPI formula, $\sigma^{(n)}I^n$, does not fit the photoionization rate with $n$ equal to the minimum number of photons required to make electrons transit to the conduction band, but with a higher order process.

## IV. WAVELENGTH DEPENDENCY

Ionization is considered to be one of the key effects responsible for the laser damage [5]. Over the first instants of the interaction, the laser beam ionizes the optical component making electron transit from the valence band to the conduction band. These conduction-band electrons are then heated by the incident radiation and lately transfer their energy to the lattice through collisional processes. Damage occurs when the deposited laser energy is sufficient to melt, boil, or fracture the optical components. On the high-power laser facilities, such as, for example, the LMJ [14] and the NIF laser [22], we are interested by three laser wavelengths: 1053, 526.5, and 351 nm. The end of the beamline, characterized with a high-energy UV laser beam, is responsible for most of the laser damage on the optical components.

Figure 5 draws the quartz photoionization rates for linear (solid curve) and circular (crosses) polarization for these three laser wavelengths: 351 nm (black), 526.5 nm (blue), and 1053 nm (red). We observe that the two highest values of the laser wavelengths display a photoionization rate weaker for circular polarization than for linear polarization. The discrepancies between the two laser polarizations mainly originate from the weaker value of the electric field amplitude for the circular polarization (see Appendix B). The UV wavelength displays a different behavior, as no difference in the photoionization rate is observed between both laser polarizations.

TABLE I. Photoionization cross sections of the fused silica bulk for three laser wavelengths.

| $\lambda_0$ (nm) | 351 | 526.5 | 1053 |
|---|---|---|---|
| Refractive index, $n_0$ | 1.476724 | 1.460965 | 1.449763 |
| Photon number, $n$ | 3 | 4 | 8 |
| $\sigma_{\text{lin}}^{(n)}$ (s$^{-1}$ cm$^{2n-3}$/W$^n$) | $9.21 \times 10^{-8}$ | $2.72 \times 10^{-21}$ | $3.85 \times 10^{-73}$ |
| $\sigma_{\text{cir}}^{(n)}$ (s$^{-1}$ cm$^{2n-3}$/W$^n$) | $8.95 \times 10^{-8}$ | $3.56 \times 10^{-23}$ | $4.0 \times 10^{-78}$ |

Table I summarizes the photoionization cross sections of the fused silica bulk for the three laser wavelengths. These numerical values are computed with Eqs. (5)–(8). These theoretical results show that circularly and linearly polarized laser beams display equal ionization rates when the photons number needed to ionize the crystal is low.

Figure 6 draws the quartz ionization rate as a function of the laser wavelength for a linear (solid curve) and a circular polarization (crosses) by considering a laser beam intensity equal to $10^{10}$ W/cm$^2$. The red circles denote the minimum number of photons ($n$) needed to make electron transit from the valence to the conduction bands. We observe that each $n$-process transition is characterized by a decrease in the ionization rate value for both laser polarizations: it is more noticeable for linear polarization. As expected, the ionization rate decreases as the laser wavelength increases due to the higher number of photons needed to ionize the crystal. But this decrease is more pronounced for the circular polarization such that the difference between the linear and the circular polarization induced ionization rate increases with the laser wavelength.

## V. COMPARISON WITH EXPERIMENTAL DATA

We now apply our theoretical development of the crystal photoionization rates to the experimental measurements

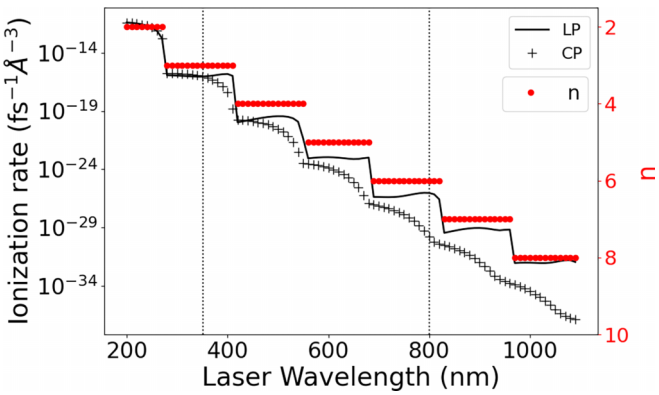


FIG. 6. Ionization rate versus the laser wavelength for a laser intensity equal to $10^{10}$ W/cm$^2$ with a linear (solid curve) and a circular (crosses) polarization. The red circles (associated with the right $y$ axis) display the number of photons ($n$) needed to make electron transit from the valence to the conduction band. Vertical dashed lines highlight laser wavelengths equal to 351 and 800 nm.

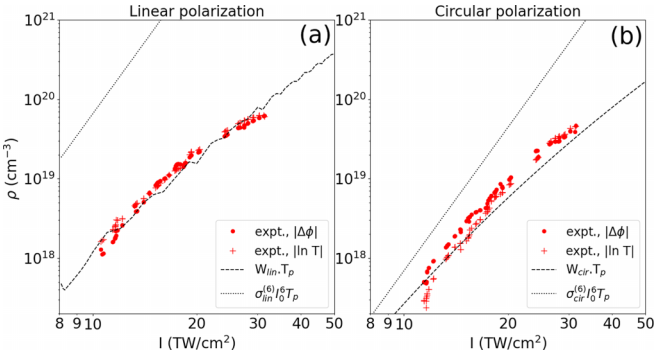


FIG. 7. Free-carrier density in fused silica measured experimentally (red circles and crosses) and computed theoretically (dashed curve) with a linearly (a) and circularly (b) polarized laser beam.

performed by Temnov *et al.* in [9]. The authors reported time-resolved measurements of the concentration of free carriers in fused silica and sapphire generated by 50-fs, 800-nm, linearly and circularly polarized laser pulses. To evaluate the free-carrier density, they considered two diagnostics: the transmission of a time-delayed probe beam through the pump-irradiated sample ($T$) and the phase shift ($\Delta\phi$) of a reflected probe beam focused on the sample rear surface. These experimental data are reported in Figs. 7 and 8 with red crosses and circles, respectively. First, Fig. 7 reports free-carrier density for a fused silica sample irradiated by a linearly [Fig. 7(a)] and a circularly [Fig. 7(b)] polarized laser beam. The sample characteristics are estimated to $B_g = 9$ eV and $n_0 = 1.4533$. The theoretical charge density (dashed curve) is computed with $\rho = W_{\text{lin}} \times T_p$, where $T_p = 50$ fs and $W_{\text{lin}}$ is given in Eq. (1). A good agreement with experimental measurements is obtained by choosing a reduced mass equal to $\mu_r = 0.1m_e$. This value will be kept constant in the following. Then, the laser beam polarization is changed from linear to circular in Fig. 7(b) where the ionization rate is computed with Eq. (2). The theoretical computations still fit the intensity-dependent charge density, and reproduce the experimental measurements that is a free-carrier density lower than in the linear case. Table II summarizes the values of the photoionization cross sections for the fused silica sample. The theoretical values are computed with Eq. (5) for the linear polarization and with

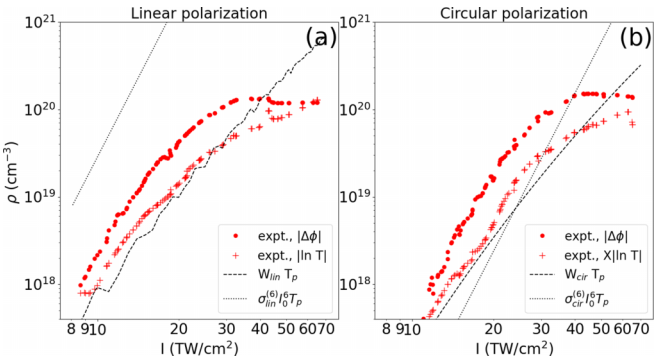


FIG. 8. Free-carrier density in sapphire measured experimentally (red circles and crosses) and computed theoretically (dashed curve) with a linearly (a) and circularly (b) polarized laser beam.

TABLE II. Comparison of the experimental and theoretical values of the fused silica photoionization cross sections for a linear and a circular polarization.

| | $\sigma_{\text{lin}}^{(6)}$ ($\text{s}^{-1}\,\text{cm}^9/\text{W}^6$) | $\sigma_{\text{cir}}^{(6)}$ ($\text{s}^{-1}\,\text{cm}^9/\text{W}^6$) |
|---|---|---|
| Experimental values | $7.5 \times 10^{-47\pm0.5}$ | $2.0 \times 10^{-47\pm0.5}$ |
| Theoretical values | $1.3169 \times 10^{-45}$ | $1.38507 \times 10^{-47}$ |

Eq. (8) for the circular polarization. Their associated free-carrier densities are drawn in Fig. 7 with dotted curves. The free-carrier density computed with the multiphoton formula largely overestimates the experimental and the theoretical values for the linear polarization. This shows that for these laser intensity values, the ionization process does not fully evolve in the multiphoton regime. In contrast to the linear case, circular polarization data display a better agreement between the multiphoton formula and the experimental and theoretical values for the free-carrier density. The theoretical value for the photoionization cross section, $1.385\,07 \times 10^{-47}$ $\text{s}^{-1}\,\text{cm}^9/\text{W}^6$, is close to that evaluated by Temnov in [9], $2.0 \times 10^{-47\pm0.5}$ $\text{s}^{-1}\,\text{cm}^9/\text{W}^6$. Then, Fig. 8 compares the free-carrier density for a sapphire sample. Without any accurate description of the sapphire bulk in [9], its characteristics are estimated from [23]: $B_g = 8.8$ eV and $n_0 = 1.7601$. Note that $\mu_r = 0.1m_e$. The theoretical values (dashed curves) for the free-carrier density present a relative agreement with the experimental measurements. However, the theory fails to reproduce the ionization saturation experimentally observed for laser intensity larger than 30–40 $\text{TW}/\text{cm}^2$. The theoretical and experimental values for the photoionization cross sections are summarized in Table III. Whereas the linear polarization displays a good agreement between theory and experiments, two orders of magnitude are observed for the circular polarization. This relative agreement between the photoionization theory and the work of Temnov *et al.* [9] is encouraging. It makes this theory reliable for studying the ionization of solid material with a circularly polarized laser beam.

## VI. CONCLUSION

By following the formalism presented in [12], we have derived the ionization rate of a parabolic two-band modeled crystal irradiated by a linearly and a circularly polarized laser beam. We observe some differences between our formula and those computed by Otobe *et al.* [12]. Nonetheless, we find that the ionization of a quartz crystal irradiated by an 800-nm laser beam is much more efficient (four orders of magnitude) for a linear polarization than for a circular polarization in the low laser intensity regime. This difference mainly originates from

TABLE III. Comparison of the experimental and theoretical values of the sapphire photoionization cross sections for a linear and a circular polarization.

| | $\sigma_{\text{lin}}^{(6)}$ ($\text{s}^{-1}\,\text{cm}^9/\text{W}^6$) | $\sigma_{\text{cir}}^{(6)}$ ($\text{s}^{-1}\,\text{cm}^9/\text{W}^6$) |
|---|---|---|
| Experimental values | $2.0 \times 10^{-46\pm0.5}$ | $3.0 \times 10^{-47\pm0.5}$ |
| Theoretical values | $5.7074 \times 10^{-46}$ | $7.52 \times 10^{-49}$ |

the dependence of the laser intensity computation with the laser polarization. However, we observe that this difference is no more valid for a UV laser beam characterized with $\lambda = 351$ nm. In this case, the dependence of the ionization rates with the laser intensity is similar for both laser polarizations. By varying the laser wavelength in the MPI regime, we show that the difference between the linear and the circular polarization induced ionization rates increases with the laser wavelength.

We have developed the ionization rate formula in the multiphoton regime and expressed it as a power of the laser intensity. This formulation provides an analytical expression for the photoionization rates in the linear and circular laser polarization. These expressions are thus easily implementable in numerical code modeling laser propagation.

By applying the theory to the experimental data reported in [9], we observe good agreement for a fused silica sample irradiated by a 50-fs, 800-nm, linearly and circularly polarized laser beam. The theory reproduces the lowering of the ionization process for a circular polarization and fits with the intensity-dependent free-carrier density. This makes the theory reliable for studying the bulk ionization under circular polarization. However, the agreement between theory and experiment is more questionable for the sapphire sample, as the theory fails to reproduce the ionization saturation around a laser intensity equal to 30–40 TW/cm$^2$. New experimental measurements of dielectric bulks ionization are required to validate or refute the theory.


## ACKNOWLEDGMENTS

The author acknowledges B. Chimier, L. Lamaignère, J.-Y. Natoli, and V. Tikhonchuk for their fruitful discussions.


## APPENDIX A: THEORETICAL DEVELOPMENT FOR THE IONIZATION RATE

$W$ denotes the ionization probability of a solid irradiated by a monochromatic plane wave. Expressed in s$^{-1}$ m$^{-3}$, it is equal to

$$W = \frac{1}{(2\pi)^3}\int d\vec{k}\lim_{T\to\infty}\frac{d\mathcal{P}_{|v\rangle\to|c\rangle}(T)}{dT}, \tag{A1}$$

where $\vec{k}$ is the Bloch wave vector, $T$ refers to the time, and $\mathcal{P}_{|v\rangle\to|c\rangle}(T)$ is the probability for an electron to transit from the valence ($|v\rangle$) to the conduction ($|c\rangle$) band. In the dipole approximation, the electron excitation probability writes as

$$\mathcal{P}_{|v\rangle\to|c\rangle}(T) = \frac{1}{\hbar^2}\left|\int_0^T \left\langle\Psi_k^{(v)}(\vec{r},t)|\vec{d}\vec{E}|\Psi_k^{(c)}(\vec{r},t)\right\rangle\right|^2, \tag{A2}$$

where $\vec{E}(\vec{r},t) = -\frac{d\vec{A}(\vec{r},t)}{dt}$ models the laser electric field with $\vec{A}(\vec{r},t)$ the potential vector, $\vec{d} = -e\vec{r}$ is the dipole term with $e$ the electron charge, and $\Psi_k^{(n)}(\vec{r},t)$ is the electronic wave function for the conduction ($n = c$) and the valence ($n = v$) bands, respectively. In analogy with the photoionization theory in solids developed by Keldysh [7] and Otobe *et al.* [12], the wave functions $\Psi_k^{(n)}(\vec{r},t)$ for the valence and conduction bands are described with the Houston function [13]:

$$\Psi_k^{(n)}(\vec{r},t) = u^{(n)}_{\vec{k}+[e\vec{A}(t)/\hbar]}(\vec{r})e^{i\{\vec{k}+[e\vec{A}(t)/\hbar]\}\vec{r}} \times e^{-(i/\hbar)\int_0^t \mathcal{E}_n(\vec{k}+[e\vec{A}(t)/\hbar])dt'}, \tag{A3}$$

where $u_{\vec{k}}^{(n)}(\vec{r})$ are the lattice periodic functions and $\mathcal{E}_n(\vec{k})$ is the associated band energy. The Houston functions satisfy the Schrödinger equation:

$$\left[\frac{[\vec{p}+\hbar\vec{k}+e\vec{A}(t)]^2}{2m_e}+V(\vec{r})\right]\Psi_k^{(n)}(\vec{r},t) = \mathcal{E}_n\left(\vec{k}+\frac{e\vec{A}(t)}{\hbar}\right)\Psi_k^{(n)}(\vec{r},t) \tag{A4}$$

with $V(\vec{r})$ the periodic lattice potential. In analogy with Otobe's work [12], we define the dipole matrix element:

$$C_{cv}(T) = \frac{e}{\hbar}\int_0^T dt\left\langle\Psi_k^{(v)}(\vec{r},t)|\vec{r}\vec{E}|\Psi_k^{(c)}(\vec{r},t)\right\rangle \tag{A5}$$

such that

$$W = \frac{2}{(2\pi)^3}\int d\vec{k}\lim_{T\to\infty}\mathrm{Re}\left[\frac{dC_{cv}^*(T)}{dT}C_{cv}(T)\right], \tag{A6}$$

where the Re($x$) function refers to the real part of $x$. By inserting Eq. (A3) into Eq. (A5), we obtain

$$C_{cv}(T) = \frac{e}{\hbar}\int_0^T dt\left\langle u^{(v)}_{\vec{k}+[e\vec{A}(t)/\hbar]}|\vec{r}|u^{(c)}_{\vec{k}'+[e\vec{A}(t)/\hbar]}\right\rangle\vec{E}e^{i(\vec{k}'-\vec{k})\cdot\vec{r}} \times e^{-(i/\hbar)\int_0^t dt'[\mathcal{E}_c(\vec{k}'+[e\vec{A}(t')/\hbar])-\mathcal{E}_v(\vec{k}+[e\vec{A}(t')/\hbar])]}. \tag{A7}$$

The dipole matrix element coupling the lattice periodic functions writes [24] as

$$\left\langle u^{(v)}_{\vec{k}+[e\vec{A}(t)/\hbar]}|\vec{r}|u^{(c)}_{\vec{k}'+[e\vec{A}(t)/\hbar]}\right\rangle = i\delta(\vec{k}-\vec{k}')\left\langle u^{(v)}_{\vec{k}}|\vec{\nabla}_{\vec{k}}|u^{(c)}_{\vec{k}}\right\rangle. \tag{A8}$$

We thus have

$$C_{cv}(T) = -i\frac{e}{\hbar}\int_0^T dt\frac{d\vec{A}(t)}{dt}\left\langle u^{(v)}_{\vec{k}}|\vec{\nabla}_{\vec{k}}|u^{(c)}_{\vec{k}}\right\rangle \times e^{-(i/\hbar)\int_0^t dt'\Delta E(\vec{k}+[e\vec{A}(t')/\hbar])}, \tag{A9}$$

where we consider a parabolic two-band system:

$$\Delta E(\vec{k}) = \mathcal{E}_c(\vec{k}) - \mathcal{E}_v(\vec{k}) \tag{A10}$$

$$= B_g + \frac{\hbar^2k^2}{2\mu_r}, \tag{A11}$$

where $B_g$ denotes the band gap and $\mu_r$ is the electron-hole reduced mass [12,25].

### 1. Linearly polarized beam

We consider a laser beam with a linear polarization:

$$\vec{A}(t) = A_0\cos(\omega t)\vec{e}_z \tag{A12}$$

leading to

$$\Delta E\left(\vec{k}+\frac{e\vec{A}(t)}{\hbar}\right)=B_g+\frac{\hbar^2k^2}{2\mu_r}+\frac{e^2A_0^2\cos^2(\omega t)}{2\mu_r}+\frac{e\hbar kA_0\cos(\omega t)}{\mu_r}\cos\theta \tag{A13}$$

with $\theta$ the angle between the $\vec{k}$ vector and the $\vec{e}_z$ axis. By inserting Eq. (A13) into Eq. (A9) and by considering $e^{im\sin(\omega t)}=\sum_{l=-\infty}^{+\infty}J_l(m)e^{il\omega t}$, where $J_l(x)$ are the Bessel functions of the first kind [17], we obtain

$$C_{cv}(T)=i\frac{eA_0\omega}{\hbar}\int_0^T dt\sin(\omega t)X_{v,c}^{(z)}\times\sum_{l,m=-\infty}^{+\infty}J_l(\alpha)J_m(\beta)e^{-(i/\hbar)[E_k-(l+2m)\hbar\omega]t}, \tag{A14}$$

$$X_{v,c}^{(z)}=\left\langle u_{\vec{k}}^{(v)}\right|\frac{\partial}{\partial k_z}\left|u_{\vec{k}}^{(c)}\right\rangle, \tag{A15}$$

$$\alpha=-\frac{eA_0k\cos\theta}{\mu_r\omega}, \tag{A16}$$

$$\beta=-\frac{e^2A_0^2}{8\mu_r\hbar\omega}, \tag{A17}$$

$$E_k=B_g+\frac{\hbar^2k^2}{2\mu_r}+\frac{(eA_0)^2}{4\mu_r}. \tag{A18}$$

This results in

$$C_{cv}(T)=i\frac{eA_0\omega}{2}X_{v,c}^{(z)}\sum_{l=-\infty}^{+\infty}[\overline{J_{l-1}}(\alpha,\beta)-\overline{J_{l+1}}(\alpha,\beta)]\times\frac{e^{-(i/\hbar)[E_k-l\hbar\omega]t}-1}{E_k-l\hbar\omega}, \tag{A19}$$

where $\overline{J_n}(u,v)$ are the generalized Bessel functions [16]. By defining $w_k=2\lim_{T\to+\infty}\mathrm{Re}[\frac{dC_{cv}^*(T)}{dT}C_{cv}(T)]$ and considering the $\lim_{T\to+\infty}\sin(xT)=\pi x\delta(x)$ formula, we obtain

$$w_k=\frac{\pi(eA_0\omega)^2}{2\hbar}\left|X_{cv}^{(z)}\right|^2\sum_{l=-\infty}^{+\infty}[\overline{J_{l-1}}(\alpha,\beta)-\overline{J_{l+1}}(\alpha,\beta)]^2\times\delta(E_k-l\hbar\omega). \tag{A20}$$

The crystal is assumed to be isotropic. Thus the dipole matrix element writes [25] as

$$\left|X_{cv}^{(z)}\right|^2=\frac{\hbar^2}{4\mu_rB_g}. \tag{A21}$$

By inserting Eq. (A21) into Eq. (A20), integrating Eq. (A20) over $\vec{k}$, and considering $\int_a^b f(x)\delta(x-x_0)=f(x_0)$ if $x\in[a,b]$, we obtain the following photoionization rate for the linear-polarized laser beam:

$$W_{\mathrm{lin}}=\frac{1}{16\sqrt{2}\pi}\frac{(eA_0\omega)^2}{\hbar^2}\frac{\mu_r^{1/2}}{B_g}\int_0^\pi\sin\theta\,d\theta\times\sum_{l\geqslant l_0}\sqrt{u_l}[\overline{J_{l-1}}(\alpha,\beta)-\overline{J_{l+1}}(\alpha,\beta)]^2, \tag{A22}$$

where $u_l=l\hbar\omega-B_g-\frac{(eA_0)^2}{4\mu_r}$, $l_0=\min_l(u_l>0)$ and $\alpha$ is transformed to $\alpha=-\frac{eA_0}{\hbar\omega}\sqrt{\frac{2}{\mu_r}}\sqrt{u_l}\cos\theta$. This equation differs from Eq. (21) in [12] by a factor $\frac{1}{2}(\frac{\hbar\omega}{Bg})^2$. The factor $\frac{1}{2}$ originates from a misprint in Eq. (21) because it is not present in the associated figure, denoted Fig. 2 in [12]. Thus, only a factor $(\frac{\hbar\omega}{Bg})^2$ differs between our result and the Otobe's result. It results from two oversights in [12]:

(1) The factor $\frac{1}{B_g}$ is forgotten in the Eq. (6) to Eq. (7) transition.

(2) The factor $\omega$ is forgotten in the Eq. (11) to Eq. (12) transition.

### 2. Circularly polarized beam

We consider a laser beam with a circular polarization:

$$\vec{A}(t)=A_0[\cos(\omega t)\vec{e}_x+\sin(\omega t)\vec{e}_y]. \tag{A23}$$

Calculations perfectly similar to Eqs. (A13)–(A19) lead to

$$C_{cv}(T)=\frac{eA_0\omega}{2\hbar}\int_0^T dt\sum_{l=-\infty}^{+\infty}e^{-(i/\hbar)[E_k-l\hbar\omega]t}e^{-il\phi}\times[M_{vc}^-J_{l-1}(\eta)e^{i\phi}-M_{vc}^+J_{l+1}(\eta)e^{-i\phi}], \tag{A24}$$

$$M_{vc}^{\pm}=\left[X_{vc}^{(x)}\pm iX_{vc}^{(y)}\right], \tag{A25}$$

$$\eta=-\frac{eA_0}{\mu_r\omega}k\sin\theta, \tag{A26}$$

$$E_k=B_g+\frac{\hbar^2k^2}{2\mu_r}+\frac{(eA_0)^2}{2\mu_r}. \tag{A27}$$

The crystal is assumed to be isotropic, such that $X_{vc}^{(x)}=X_{vc}^{(y)}=X_{vc}^{(z)}$. Thus $M_{vc}^{\pm}=X_{vc}[1\pm i]$ where $X_{vc}$ is given by Eq. (A21). We have

$$w_k=\frac{\pi(eA_0\omega)^2}{\hbar}|X_{cv}|^2\sum_{l=-\infty}^{+\infty}\left[J_{l-1}^2(\eta)+J_{l+1}^2(\eta)\right]\times\delta(E_k-l\hbar\omega), \tag{A28}$$

where the Bessel crossed terms are neglected. By integrating over the $\vec{k}$ vector, we obtain the ionization rate for a circularly polarized beam:

$$W_{\mathrm{cir}}=\frac{1}{8\sqrt{2}\pi}\frac{(eA_0\omega)^2}{\hbar^2}\frac{\mu_r^{1/2}}{B_g}\int_0^\pi\sin\theta\,d\theta\times\sum_{l\geqslant l_0}\sqrt{u_l}\left[J_{l-1}^2(\eta)+J_{l+1}^2(\eta)\right] \tag{A29}$$

with $u_l=l\hbar\omega-B_g-\frac{(eA_0)^2}{2\mu_r}$, $l_0=\min_l(u_l>0)$ and $\eta$ is transformed to $\eta=-\frac{eA_0}{\hbar\omega}\sqrt{\frac{2}{\mu_r}}\sqrt{u_l}\sin\theta$. In a similar way as the linear polarization, our result differs from Eq. (16) in [12] by a $(\frac{\hbar\omega}{Bg})^2$ factor.

## APPENDIX B: LASER INTENSITY AND ELECTRIC FIELD AMPLITUDE

The potential vector modeling the $z$-propagating linearly or circularly polarized laser beam writes as

$$\vec{A}(t) = A_0[\cos(\omega t - kz)\vec{e}_x + \chi \sin(\omega t - kz)\vec{e}_y], \quad \text{(B1)}$$

where $\chi = 0, 1$ for linear and circular polarization, respectively. Note that the electric field amplitude is equal to $E_0 = \omega A_0$.

Averaged over one optical period, the laser energy density $\rho(v) = \frac{1}{2}[\epsilon|\vec{E}|^2 + \frac{1}{\mu_0}|\vec{B}|^2]$ writes as

$$\rho(v) = \tfrac{1}{2}\epsilon_0 n_0^2 E_0^2[1 + \chi^2] \quad \text{(B2)}$$

with $\epsilon_0$ the vacuum permittivity and $n_0$ the linear refractive index. The laser intensity, defined by $I = \rho(v)\frac{c}{n_0}$, with $c$ the light speed in vacuum, is equal to

$$I = \tfrac{1}{2}\epsilon_0 c n_0 E_0^2[1 + \chi^2]. \quad \text{(B3)}$$

We retrieve the well-known feature concerning a circularly polarized laser beam: for a defined laser intensity, the electric field amplitude of a circularly polarized laser beam is lower than the linearly polarized one by a factor $\sqrt{2}$.

## APPENDIX C: DISPERSION LAW FOR A QUARTZ CRYSTAL

Throughout the document, we compute the linear refractive index of the crystal with the following dispersion law [18]:

$$n_0^2 - 1 = \frac{0.696\,166\,3 \times \lambda_{\mu m}^2}{\lambda_{\mu m}^2 - 0.068\,404\,3^2} + \frac{0.407\,942\,6 \times \lambda_{\mu m}^2}{\lambda_{\mu m}^2 - 0.116\,241\,4^2} + \frac{0.897\,479\,4 \times \lambda_{\mu m}^2}{\lambda_{\mu m}^2 - 9.896\,161^2}, \quad \text{(C1)}$$

where $\lambda_{\mu m}$ is the laser wavelength expressed in micrometers.


[1] E. G. Gamaly and A. V. Rode, Physics of ultra-short laser interaction with matter: From phonon excitation to ultimate transformations, Prog. Quantum Electron. **37**, 215 (2013).

[2] D. Tan, K. N. Sharafudeen, Y. Yue, and J. Qiu, Femtosecond laser induced phenomena in transparent solid materials: Fundamentals and applications, Prog. Mater. Sci. **76**, 154 (2016).

[3] P. Balling and J. Schou, Femtosecond-laser ablation dynamics of dielectrics: basics and applications for thin films, Rep. Prog. Phys. **76**, 036502 (2013).

[4] H. Yang, J. Cheng, Z. Liu, Q. Liu, L. Zhao, J. Wang, and M. Chen, Dynamic behavior modeling of laser-induced damage initiated by surface defects on KDP crystals under nanosecond laser irradiation, Sci. Rep. **10**, 500 (2020).

[5] B. C. Stuart, M. D. Feit, S. Herman, A. M. Rubenchik, B. W. Shore, and M. S. Perry, Nanosecond-to-femtosecond laser induced breakdown in dielectrics, Phys. Rev. B **53**, 1749 (1996).

[6] S. Nisar, L. Li, and M. A. Sheikh, Laser glass cutting techniques—A review, J. Laser Appl. **25**, 042010 (2013).

[7] L. V. Keldysh, Ionization in the field of a strong electromagnetic wave, Sov. Phys. JETP **20**, 1307 (1965).

[8] V. E. Gruzdev, Analysis of Keldysh's formula for the ionization rate in solids, in *Proceedings of SPIE Nonresonant Laser-Matter Interaction*, edited by M. N. Libenson (SPIE, Bellingham, WA, 2004), Vol. 5506, page 138.

[9] V. V. Temnov, K. Sokolowski-Tinten, P. Zhou, A. El-Khamhawy, and D. von der Linde, Multiphoton Ionization in Dielectrics: Comparison of Circular and Linear Polarization, Phys. Rev. Lett. **97**, 237403 (2006).

[10] E. L. Ivchenko and E. Y. Perlin, Polarization properties of many-photon interband absorption of light in cubic crystals, Sov. Phys. Solid State **15**, 1850 (1973).

[11] H. D. Jones and H. R. Reiss, Intense-field effects in solids, Phys. Rev. B **16**, 2466 (1977).

[12] T. Otobe, Y. Shinohara, S. A. Sato, and K. Yabana, Theory for electron excitation in dielectrics under an intense linear and circularly polarized laser fields, J. Phys. Soc. Jpn. **88**, 024706 (2019).

[13] W. V. Houston, Acceleration of electrons in a crystal lattice, Phys. Rev. **57**, 184 (1940).

[14] J.-L. Miquel, C. lion, and P. Vivini, The Laser Mega-Joule: LMJ & PETAL status and program overview, J. Phys.: Conf. Ser. **688**, 012067 (2016).

[15] C. Kittel, *Introduction to Solid States Physics* (Wiley, New York, 2005).

[16] H. R. Reiss and V. P. Krainov, Generalized Bessel functions in tunneling ionization, J. Phys. A: Math. Gen. **36**, 5575 (2003).

[17] M. Abramowitz and I. A. Stegun, *Handbook of Mathematical Functions with Formulas, Graphs, and Mathematical Tables* (National Bureau of Standards, Washington, D.C., 1972).

[18] I. H. Malitson, Interspecimen comparison of the refractive index of fused silica, J. Opt. Soc. Am. **55**, 1205 (1965).

[19] S. Klarsfeld and A. Maquet, Circular versus Linear Polarization in Multiphoton Ionization, Phys. Rev. Lett. **29**, 79 (1972).

[20] A. M. Perelomov, V. S. Popov, and M. V. Terent'ev, Ionization of atoms in an alternating electric field, Sov. Phys. JETP **23**, 924 (1966).

[21] M. V. Amnosov, N. B. Delone, and V. P. Krainov, Tunnel ionization of complex atoms and atomic ions in an alternating electromagnetic field, Sov. Phys. JETP **64**, 1191 (1986).

[22] C. A. Haynam, P. J. Wegner, J. M. Auerbach, M. W. Bowers, S. N. Dixit, G. V. Erbert, G. M. Heestand, M. A. Henesian, M. R. Hermann, K. S. Jancaitis *et al.*, National ignition facility laser performance status, Appl. Opt. **46**, 3276 (2007).

[23] F. Quéré, S. Guizard, and Ph. Martin, Time-resolved study of laser-induced breakdown in dielectrics, Europhys. Lett. **56**, 138 (2001).

[24] B. Gu, N. H. Kwong, and R. Binder, Relation between the interband dipole and momentum matrix elements in semiconductors, Phys. Rev. B **87**, 125301 (2013).

[25] E. O. Kane, Zener tunneling in semiconductors, J. Phys. Chem. Solids **12**, 181 (1960).


*Correction:* The previously published Figure 5 contained incorrect units on the $y$ axis and has been replaced.